J|A|C|S ARTICLES

Published on Web 09/24/2010

An Original Polymorph Sequence in the High-Temperature Evolution of the Perovskite Pb_2TmSbO_6

Sebastián A. Larrégola,[†] José A. Alonso,[*,‡] Denis Sheptyakov,[§] Miguel Algueró,[‡] Angel Muñoz,[||] Vladimir Pomjakushin,[§] and José C. Pedregosa[†]

Área de Química General e Inorgánica, Departamento de Química, Facultad de Química, Bioquímica y Farmacia, Universidad Nacional de San Luis, Chacabuco y Pedernera, 5700 San Luis, Argentina, Instituto de Ciencia de Materiales de Madrid, C.S.I.C., Cantoblanco, 28049 Madrid, Spain, Laboratory for Neutron Scattering, PSI Villigen, CH-5232 Villigen PSI, Switzerland, and Dpto. de Física Aplicada, EPS, Universidad Carlos III, Avda. Universidad 30, E-28911, Leganés-Madrid, Spain

Received May 30, 2010; E-mail: ja.alonso@icmm.csic.es

Abstract: The synthesis, crystal structure, and dielectric properties of the novel double perovskite Pb_2TmSbO_6 are described. The room-temperature crystal structure was determined by ab initio procedures from neutron powder diffraction (NPD) and synchrotron X-ray powder diffraction (SXRPD) data in the monoclinic *C*2/*c* (No. 15) space group. This double perovskite contains a completely ordered array of alternating TmO_6 and SbO_6 octahedra sharing corners, tilted in antiphase along the three pseudocubic axes, with an $a^-b^-b^-$ tilting scheme, which is very unusual in the crystallochemistry of perovskites. The lead atoms occupy a highly asymmetric void with 8-fold coordination due to the stereoactivity of the Pb^{2+} lone electron pair. This compound presents three successive phase transitions in a narrow temperature range (at $T1 = 385$ K, $T2 = 444$ K, and $T3 = 460$ K in the heating run) as shown by differential scanning calorimetry (DSC) data. The crystal structure and temperature-dependent NPD follow the space-group sequence $C2/c \rightarrow P2_1/n \rightarrow R\bar{3} \rightarrow Fm\bar{3}m$. This is a novel polymorph succession in the high-temperature evolution of perovskite-type oxides. The Tm/Sb long-range ordering is preserved across the consecutive phase transitions. Dielectric permittivity measurements indicate the presence of a paraelectric/antiferroelectric transition (associated with the last structural transition), as suggested by the negative Curie temperature obtained from the Curie−Weiss fit of the reciprocal permittivity.

1. Introduction

The perovskite-type oxides exhibit the general formula ABO_3, where A represents a large electropositive cation and B stands for a small transition metal ion. The prototypical perovskite structure (aristotype) is cubic, and it can be described as a framework of corner-sharing BO_6 octahedra with the A cations located at the 12-fold coordinated voids within the octahedra. The so-called double perovskite $A_2B'B''O_6$ oxides contain two suitable B′ and B″ cations at the octahedral positions. Double perovskites may present different kinds of cationic ordering at the octahedral sites as it has been reviewed by Anderson et al.[1] The most common ordering is a rock-salt arrangement of the $B'O_6$ and $B''O_6$ octahedra in a perfectly alternated disposition along the three directions of the crystal. The layered ordering is another possibility, which is mostly observed in copper-containing perovskites, where alternating layers of $B'O_6$ and $B''O_6$ octahedra compose the crystal structure.

The tolerance factor for $A_2B'B''O_6$ double perovskites is defined as $t = (r_A + r_O)/[\sqrt{2}[(r_{B'} + r_{B''})/2 + r_O]]$. The ideal double perovskite also shows a cubic symmetry ($t = 1$), space group $Fm\bar{3}m$, with a doubled unit-cell edge with respect to that of the ABO_3 aristotype. If there is a mismatch between the A−O and the average (B′,B″)−O bond lengths, that is, $t < 1$ or $t > 1$, the structure of the double perovskites experiences a distortion from the cubic symmetry, giving rise to a superstructure. Just like ABO_3 perovskites, the most frequent distortions in $A_2B'B''O_6$ oxides are due to the tilting of the $B'O_6/B''O_6$ octahedra. On the basis of Glazer's description of the tilt systems, Woodward[2] has considered the cation ordering and octahedral tilting occurring simultaneously and derived 13 possible space groups for double perovskites. Howard et al.[3] identified, using the group-theoretical analysis, 12 space groups under the same conditions of octahedral tilting and cation ordering. Despite such a theoretical variability, only a few space groups have been actually observed in the real world, that is, $a^0a^0a^0$ ($Fm\bar{3}m$), $a^0a^0c^-$ ($I4/m$), $a^-a^-a^-$ ($R\bar{3}$), $a^0b^-b^-$ ($I2/m$), and $a^-a^-b^+$ ($P2_1/n$). In addition, for many double perovskites the deviation from the ideal cubic structure (due to compositional, temperature, or pressure changes) in general follows either the sequence $Fm\bar{3}m \rightarrow I4/m \rightarrow I2/m \rightarrow P2_1/n$ or the sequence $Fm\bar{3}m \rightarrow R\bar{3} \rightarrow I2/m \rightarrow P2_1/n$.

[†] Universidad Nacional de San Luis.
[‡] C.S.I.C.
[§] ETH Zurich and PSI Villigen.
[||] Universidad Carlos III.

(1) Anderson, M. T.; Greenwood, K. B.; Taylor, G. A.; Poeppelmeier, K. R. *Prog. Solid State Chem.* **1993**, *22*, 197.
(2) Woodward, P. M. *Acta Crystallogr., Sect. B* **1997**, *53*, 32.
(3) Howard, C. J.; Kennedy, B. J.; Woodward, P. M. *Acta Crystallogr., Sect. B* **2003**, *59*, 463A.

10.1021/ja104417f

Double-perovskite oxides have attracted a great interest in recent years, mainly due to their appealing physical properties, such as superconductivity,[4,5] dielectricity,[6,7] or magnetoresistivity.[8] Among them, the lead-based double perovskites of formula $Pb_2B'B''O_6$ combine some exotic properties with an unusual structural evolution. In distorted perovskites, the symmetry can be monoclinic, as it happens in incommensurate Pb_2CoWO_6[9] and Pb_2CdWO_6,[10] or orthorhombic as in antiferroelectric Pb_2MgWO_6[11] and Pb_2YbNbO_6.[12,13] There are some exceptions, which include Pb_2MgTeO_6,[14] in which the main distortion is trigonal, as it happens in B-site disordered perovskites, and Pb_2CoTeO_6[15] that presents, at room temperature, a tetragonally distorted perovskite structure, with unit-cell parameters $a = b = 5.661(5)$, $c = 8.004(7)$ Å, S.G. *I4/mmm* ($Z = 2$). Among the orthorhombic phases, just two types of superstructures have been found so far. The superstructure of Pb_2MgWO_6 is representative of the first class, only observed for $Pb_2B'^{2+}B''^{6+}O_6$ compounds. It is characterized by two modulation wavevectors.[11] The second superstructure belongs to $Pb_2B'^{3+}B''^{5+}O_6$ oxides as, for example, Pb_2YbNbO_6, which is characterized by only one modulation wavevector.[13] In this case, Pb atoms are reported to be shifted along the (110) cubic direction, whereas in Pb_2MgWO_6 the Pb shift happens along (100). However, no complete structural determination has been described for any $Pb_2B'^{3+}B''^{5+}O_6$ compound, so an experimentally well-assessed comparison with the $Pb_2B'^{2+}B''^{6+}O_6$ family has not been established.

Some members of the $Pb_2B'^{3+}B''^{5+}O_6$ family present really interesting physical properties: Lead ytterbium tantalate Pb_2YbTaO_6 is an antiferroelectric similar to Pb_2YbNbO_6 and Pb_2HoNbO_6 perovskites.[16] The room temperature (RT) phase symmetry is interpreted as an orthorhombically distorted ABO_3-type subcell, and the space group for both antiferroelectric (AFE) and ferroelectric (FE) phases is considered to be *Pbnm*.[17−20] It has also been observed that the specimen shows weak relaxor behavior at the AFE−FE phase transition, and the existence of nanopolar regions is assumed to be the responsible factor for the relaxor behavior.[21]

In the present work, we have prepared, for the first time, and characterized a new member of the $Pb_2B^{3+}B^{5+}O_6$ family, the Pb_2TmSbO_6 perovskite. It presents a rare room-temperature crystal structure and three successive phase transitions as a function of temperature, across a novel series of polymorphs, which have been investigated by neutron and X-ray diffraction, complemented with the measurement of the dielectric properties. This Article reports on the structural evolution of this novel member of the perovskite family.

2. Experimental Section

a. Synthesis. Pb_2TmSbO_6 was obtained by standard solid-state techniques; PbO, Tm_2O_3, Sb_2O_3 were used as starting materials. They were weighed out in the appropriate metal ratios and well mixed in an agate mortar. The mixture was calcined at 550 C for 24 h in air to oxidize Sb^{3+} to Sb^{5+}. Subsequently, the product was heated at 800 and 900 C for 12 h in air until a single Pb_2TmSbO_6 phase was obtained. All thermal treatments were carried out in sintered alumina crucibles.

b. Powder Diffraction Data Collection. In the global structural characterization of the sample, several diffraction techniques have been used. From XRPD data, the oxygen location cannot be determined accurately in the presence of heavy atoms such as Pb and Tm; thus a NPD study was essential to investigate the structural features of this perovskite, neutrons being more sensitive to the oxygen positions. Temperature-dependent X-ray and neutron diffraction experiments have been carried out to study the crystal structure evolution.

The initial structural identification and characterization of the sample was carried out by laboratory X-ray powder diffraction (XRPD) in a Bruker D8 Advance powder diffractometer in the Bragg−Brentano geometry. Temperature-dependent powder X-ray diffraction patterns were collected with the same equipment provided with a commercial heating chamber (Anton Paar). These patterns were recorded with Cu K_α radiation in the temperature range RT < T < 558 K. It must be pointed out that some temperature gradient is observed by inaccuracy of the heating control; in fact, the phase transitions were systematically detected at higher temperatures at the XRPD experiments.

NPD data were collected at the HRPT high-resolution diffractometer ($\lambda = 1.494$ Å) in the PSI (Switzerland). About 4 g of sample was placed in a vanadium can, and the counting time was typically 3 h per pattern. For the thermal evolution study, several patterns have been collected in the temperature range RT < T < 463 K. In addition, a synchrotron X-ray powder diffraction (SXRPD) experiment has been carried out at the Powder Diffraction Station of the Materials Sciences (MS-Powder) beamline at the Swiss Light Source,[22] with the use of the Microstrip Detector Mythen-II. The diffraction pattern was collected at RT with the powder sample enclosed in the glass capillary with a diameter 0.3 mm. The X-ray wavelength was $\lambda = 0.82658$ Å.

c. Differential Scanning Calorimetry (DSC). Differential scanning calorimetry (DSC, measured with Netzsch DSC 204F1 device) measurements were performed during the heating and cooling runs from RT to 557 K with a rate of 5 K min^{-1} using a 20.24 mg powder sample encapsulated in standard Al crucibles. An argon stream was used during the whole experiment as protecting gas.

d. Dielectric Permittivity Measurements. The sample has been cold-pressed at 2 GPa, then sintered at moderate temperatures (1073 K), to avoid the modification of the stoichiometry of the sample due to volatilization losses of PbO. Ag electrodes were painted on the major faces of thinned ceramic discs and sintered at 873 K for electrical characterization. The thermal dependence of the dielectric permittivity was measured above RT up to 700 K with a HP4284A precision LCR meter. Measurements were dynamically carried out

(4) Sleight, W.; Gillson, J. L.; Bierstedt, P. E. *Solid State Commun.* **1975**, *17*, 27.
(5) Cox, D. E.; Sleight, A. W.; Moon, R. M. *Proc. Conf. Neutron Scattering, National Technical Information Service, Springfield, VA, Gatlinburg* **1976**, 45.
(6) Akbas, M. A.; Davies, P. K. *J. Am. Ceram. Soc.* **1998**, *81*, 670.
(7) Reaney, I. M.; Colla, E. L.; Setter, N. *Jpn. J. Appl. Phys.* **1994**, *33*, 3984.
(8) Kobayashi, K.-I.; Kimura, T.; Sawada, H.; Terakura, K.; Tokura, Y. *Nature (London)* **1998**, *395*, 677.
(9) Sciau, Ph.; Calvarin, G.; Sun, B. N.; Schmid, H. *Phys. Status Solidi A* **1992**, *129*, 309.
(10) Sciau, Ph.; Grebille, D. In *Aperiodic '94*; Chapuis, G., Paciorek, W., Eds.; World Scientific: Singapore, 1995; p 460.
(11) Baldinozzi, G.; Sciau, Ph.; Buffat, P. A. *Solid State Commun.* **1993**, *86*, 541.
(12) Kwon, J. R.; Choo, W. K. *J. Phys.: Condens. Matter* **1991**, *3*, 2147.
(13) Choo, W. K.; Kim, H. J.; Yang, J. H.; Lim, H.; Lee, J. Y.; Kwon, J. R.; Chun, C. H. *Jpn. J. Appl. Phys.* **1993**, *32*, 4249.
(14) Baldinozzi, G.; Sciau, Ph.; Moret, J.; Buffat, P. A. *Solid State Commun.* **1994**, *89*, 441.
(15) Wedel, B.; Müller-Buschbaum, Hk. *Z. Naturforsch., B* **1997**, *52*, 35.
(16) Yasuda, N.; Konda, J. *Appl. Phys. Lett.* **1993**, *62*, 535.
(17) Park, Y. *J. Phys. Chem. Solids* **1998**, *59*, 1423.
(18) Park, S. B.; Choo, W. K. *Jpn. J. Appl. Phys.* **2000**, *39*, 5560.
(19) Park, Y.; Cho, K. *J. Am. Ceram. Soc.* **2000**, *83*, 135.
(20) Sciau, P.; Lampis, N.; Lehmann, A. G. *Solid State Commun.* **2000**, *116*, 225.
(21) Rout, D.; Subramanian, V.; Hariharan, K.; Sivasubramanian, V.; Murthy, V. R. K. *Ferroelectrics* **2004**, *300*, 67.
(22) http://sls.web.psi.ch/view.php/beamlines/ms/pd/index.html.

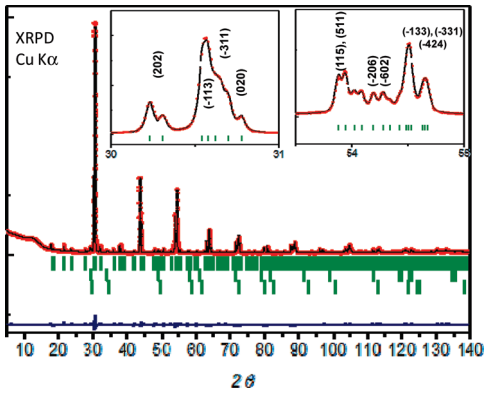

Figure 1. XRPD Rietveld plot for Pb_2TmSbO_6 in the *C*2/*c* space group at RT. Observed (red ●), calculated (solid line), and difference (bottom). The second and third rows of tick lines represent the Bragg reflections of the impurities. Inset: Indexation of the split peaks from the prototypical (110) and (211) reflections of the basic ABO_3.

during a heating/cooling cycle at ±2 K min^{-1} rate at nine frequencies between 100 Hz and 1 MHz.

e. Structural Refinements. The refinements of the crystal structures were performed by the Rietveld method using the program Fullprof.[23] The peak profiles were fitted by the Thompson−Cox−Hastings pseudo-Voigt function corrected for axial divergence asymmetry. The RT crystal structure has been refined from the joint NPD and SXRPD data, while its thermal evolution has been followed from NPD data. The following parameters were refined in the final run for each fit: scale factor, background coefficients, zero-point error, pseudo-Voigt corrected for asymmetry parameters, positional coordinates, isotropic displacement parameters, Tm/Sb antisite disordering, and occupancy factors for oxygen and lead atoms. The neutron coherent scattering lengths for Pb, Tm, Sb, and O are 9.405, 7.07, 5.57, and 5.803 fm, respectively.

3. Results

Pb_2TmSbO_6 was obtained as a well-crystallized light-yellowish polycrystalline sample. A laboratory XRPD diagram collected at RT is shown in Figure 1; the structure is refined according to the model described in the section 3.3. The pattern is characteristic of a perovskite structure, exhibiting superstructure peaks due to the long-range ordering of the B-site cations. Two minor impurities of PbO_2 with a slightly different composition have been detected with a weight fraction of less than 2%.

3.1. DSC and Dielectric Permittivity Measurements. Differential scanning calorimetry (DSC) curves are plotted in Figure 2 in the heating and cooling runs between 298 and 500 K. The appearance of three consecutive endothermic processes is observed upon heating. These thermal events are reversible as shown in the cooling curve. The heating/cooling temperatures of the successive processes are 385/379 K, 444/441 K, and 460/459 K. The three phase transition enthalpies calculated from the DSC peaks as $\Delta H = \int \Delta C_p \, dT$ were $\Delta_1 H$ = 813 J/mol, $\Delta_2 H$ = 1425 J/mol, and $\Delta_3 H$ = 114.4 J/mol.

To analyze the order of the phase transitions and to avoid the heating/cooling rate effect in the peak positions, we have measured different heating and cooling runs at four rates (3, 5, 7, and 10 K min^{-1}). Clear shifts of the peaks associated with the three phase transitions are observed in Figure S.1a. The dependence of the ΔT for each peak versus the heating/cooling rate is plotted in Figure S.1b. The extrapolation to zero rate

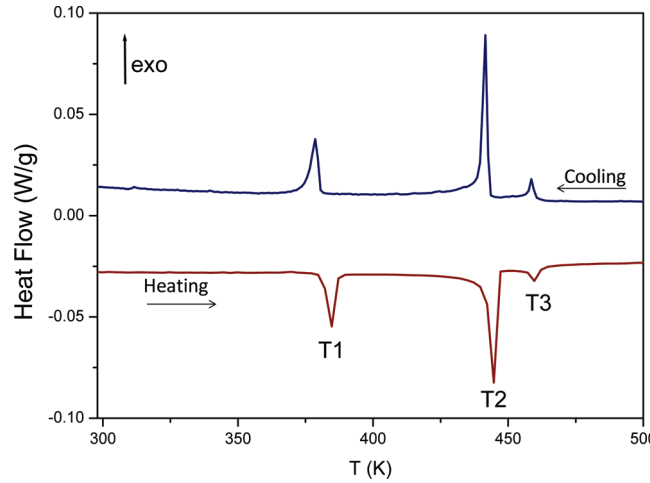

Figure 2. DSC plot. Endothermic peaks correspond to the heating process, while exothermic peaks correspond to the cooling run.

from a linear regression of the data gives us the thermal hysteresis of the process. The obtained hysteresis from the linear fits were 4.6 ± 0.5, 1.8 ± 0.3, and −0.2 ± 0.3 K for *T*1, *T*2, and *T*3, respectively. The first two values indicate significantly hysteretic first-order phase transitions, while for *T*3 no hysteresis is present (within the experimental error), suggesting a second-order process.

These measurements unveil the existence of four polymorphic phases in the explored temperature range. From the thermodynamic values (associated enthalpies), all the processes correspond to displacive phase transitions, which are typically observed in perovskite compounds.

The dielectric permittivity for the Pb_2TmSbO_6 ceramic sample, measured during a heating/cooling cycle between RT and 700 K, is shown in Figure 3a at 1 MHz. Three clear dielectric anomalies are associated with the three successive phase transitions described above. Specific temperatures are better determined from the derivative plot, shown in Figure 3b. From RT up to high temperature, the material seems to undergo a strongly first-order phase transition at 384 and 392 K on the heating and cooling runs, respectively, and two transitions with little thermal hysteresis at ∼473 and 457 K, respectively. No hysteresis loops have been carried out in the entire temperature range because strong high-field conduction was found. Dielectric losses are given in Figure S.2 in the Supporting Information to illustrate this issue.

Finally, dielectric permittivity measurements show that the high-temperature transition at *T*3 ≈ 473 K might be a polar transition as indicated by the good fit of the temperature dependence of the permittivity above 550 K to a Curie−Weiss behavior, shown in Figure S.3. The dielectric permittivity was measured at a highest frequency of 1 MHz because the material presented non-negligible conductivity that resulted in high temperature dispersion, also clearly shown in the figure. A Curie−Weiss constant of 2.1 × 10^{-5} K was obtained, in the typical range for displacive ferroelectric transitions, and very close to that of $BaTiO_3$.[24] However, the observed negative Curie−Weiss temperature (−787 K) suggests an antiferroelectric/paraelectric transition.[25]

3.2. X-ray Thermo-diffractometry. To analyze the actual nature of the phases after the anomalies detected by DSC and

(23) Rodríguez-Carvajal, J. *Physica B* **1993**, *55*, 192.

(24) Lines, M. E.; Glass, A. M. *Principles and Applications of Ferroelectric and Related Materials*; Clarendon Press: Oxford, 1977.

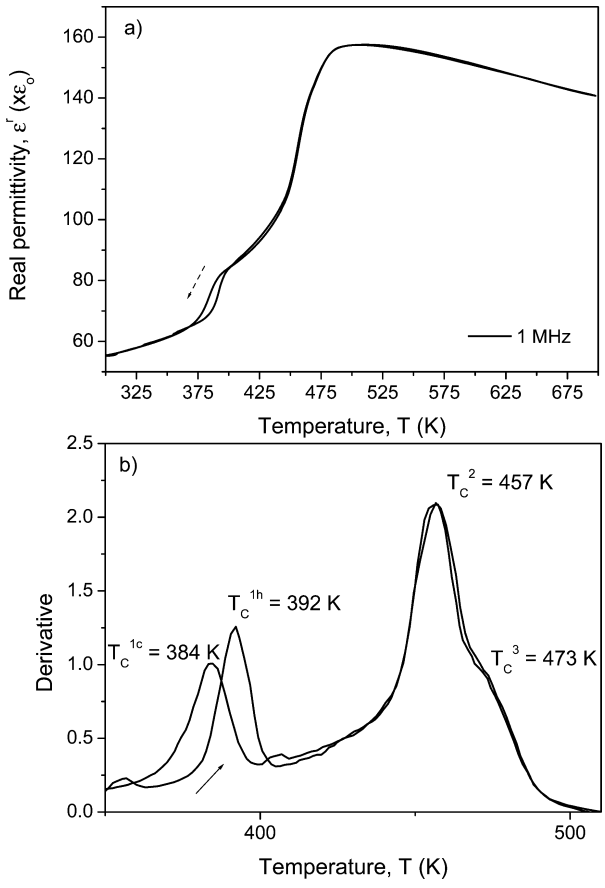

Figure 3. (a) Temperature dependence of the real permittivity of Pb_2TmSbO_6 at 1 MHz. (b) Derivative curve of the real permittivity data. Arrows indicate the temperature progression.

dielectric permittivity data, the thermal evolution of the XRPD patterns was investigated between RT and 558 K. It must be noted that the phase transition temperatures determined by the XRPD experiment are shifted from those obtained by the other characterization experiments due to the inaccuracy of the temperature control in the high-temperature chamber. Figure 4 shows the evolution of the splitting of the basic reflections (110), (200), and (211) of the XRPD patterns measured for the four different polymorphic phases. The XRPD pattern at RT after the cooling run is identical to the original pattern (see Figure S.4 and Table S.I in the Supporting Information); this fact evidences the reversibility of all the phase transitions presented by the Pb_2TmSbO_6 perovskite.

3.3. Structural Analysis. The Goldschmidt tolerance factor calculated for Pb_2TmSbO_6 using the effective ionic radii[26] for $^{VIII}Pb^{2+}$, $^{VI}Tm^{3+}$, and $^{VI}Sb^{5+}$ cations and $^{VI}O^{2-}$ is $t = 0.89$, sufficiently below unity to give rise to deviations from the cubic symmetry. The reduction in symmetry is mainly due to subtle tilts of the BO_6 octahedra, involving small shifts of the oxygen positions, which can be suitably detected by neutron diffraction.

Four different polymorphs of Pb_2TmSbO_6 were identified as a function of the temperature, in agreement with the observed DSC peaks. In the temperature range from RT to 383 K, the P_α polymorph is observed; in the temperature interval between 383 and 443 K, a second polymorph, hereafter called P_β, is identified; finally, in the narrow interval from 443 to 458 K, the P_γ polymorph is stabilized; and at temperatures higher than 458 K, a cubic double perovskite (P_δ) is identified.

Alpha Polymorph (P_α). The RT crystal structure of Pb_2TmSbO_6 was resolved ab initio from XRPD data, and subsequently refined from combined high-resolution NPD and SXRPD data. The XRPD pattern was indexed with the TOPAS software[27] from Bruker AXS in a perovskite superstructure with unit-cell parameters related to the ideal cubic perovskite aristotype ($a_0 \approx 4$ Å) as $a \approx c \approx \sqrt{6}a_0$, and $b \approx \sqrt{2}a_0$. The systematic extinctions were consistent with the *C*2/*c* space group (No. 15).[28] The inset of Figure 1 illustrates the splitting of the prototypical reflections (110) and (211) of the ABO_3 aristotype, indexed in the mentioned unit cell. Finally, the structure was solved with the FOX[29] software. The mentioned space group is also given by the SPUDS program[30] as corresponding to the $a^-b^-b^-$ tilting system. In the corresponding structural model, Tm and Sb atoms are located at the 4e ($0y^1/_4$) and 4c ($^1/_4{}^1/_40$) Wyckoff sites, respectively, the oxygen atoms occupy three crystallographically

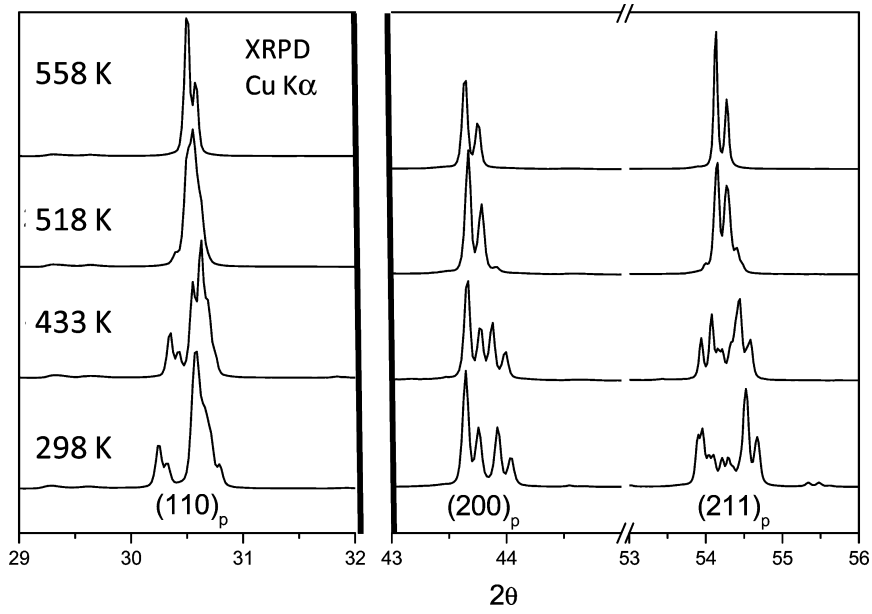

Figure 4. Thermal evolution of the XRPD patterns showing the progression of the splitting of the (110), (200), and (211) pseudocubic reflections for the four polymorphic phases.

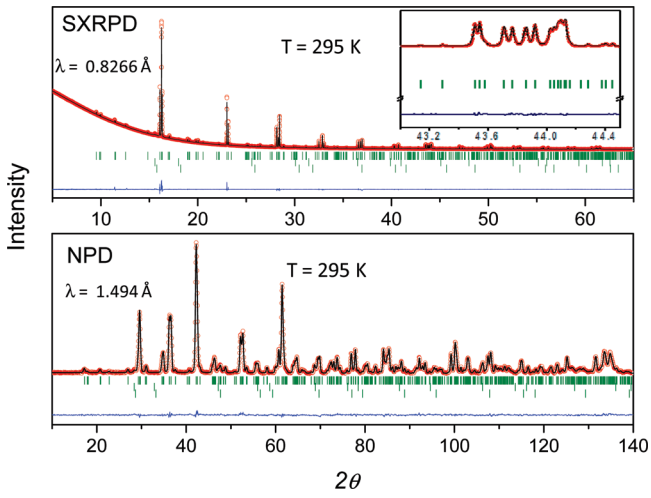

Figure 5. Observed (red ●), calculated (solid line), and difference (bottom) profiles after a joint refinement for the RT polymorph P_α: (a) SXRPD data. Inset: Close-up illustrating the exceptional agreement reached for the synchrotron pattern. (b) High-resolution NPD data.

nonequivalent positions located at 8f (*xyz*), and Pb atoms are also placed at the 8f (*xyz*) Wyckoff sites. In this model, there are four Pb_2TmSbO_6 chemical formulae per unit cell ($Z = 4$). The determined unit-cell parameters after the refinement were $a = 10.1523(3)$ Å, $b = 5.8224(1)$ Å, $c = 10.1379(3)$ Å, and $\beta = 108.729(1)$. In P_α, each TmO_6 octahedron is surrounded by six SbO_6 octahedra and vice versa; in fact, the alternated TmO_6 and SbO_6 units display antiphase tilting along the [100], [010], and [001] directions of the pseudocubic cell. As mentioned above, this tilt pattern corresponds to the $a^-b^-b^-$ Glazer notation as derived by Woodward[2] for 1:1 ordering in double perovskites. Figure 5 shows the Rietveld refinement plots for both SXRPD and NPD data sets, exhibiting an excellent agreement between observed and calculated profiles. Table 1 lists the unit-cell parameters, atomic positions, anisotropic thermal factors, and reliability factors. In addition, Table 2 contains the main bond lengths and some selected bond angles. Figure 6 displays a perspective of the P_α structure and the three pseudocubic directions (marked with the subscript p) along which the octahedral tilting occurs.

Beta Polymorph (P_β). The structural determination of the P_β polymorph has been carried out from the NPD data collected at $T = 400$ K, after the first DSC peak. The crystal structure of P_β has been indexed from X-ray laboratory data in a monoclinic unit cell, space group $P2_1/n$ (No. 14), $Z = 2$. The unit-cell parameters obtained from the refinement were $a = 8.2679(1)$ Å, $b = 5.8444(1)$ Å, $c = 5.9007(1)$ Å, and $\beta = 90.172(1)$; these parameters are related to the a_0 lattice constant of the aristotype as $b \approx c \approx \sqrt{2}a_0$ and $a \approx 2a_0$. The atomic positions in this model are given in Table 3. The overall fit between observed and calculated profiles was very good as shown in Figure 7a; however, there exist two tiny peaks (only appearing between $T1$ and $T2$), which cannot be fitted by the mentioned model (see the inset of Figure 7a). The positions of these peaks in the XRD patterns significantly evolve with temperature between $T1$ and $T2$, as illustrated in Figure 8. Taking into account that the $P2_1/n$ refinement describes very satisfactorily all the remaining peaks in the pattern, we assume that these unsolved peaks that shift with temperature may indicate that we are in the presence of an incommensurate structure, which can be described as a first approximation by a $P2_1/n$ model (commensurate subcell). The indexation of the incommensurate peaks, by using the *k*-search software of the Fullprof suite, is consistent with a modulation wavevector $q = [{}^1/_2 0 {}^1/_3]$; however, a most precise determination of the peculiarities of this polymorph remains an open issue for the time being. Table 3 includes the unit-cell parameters, atomic positions, isotropic thermal factors, occupancy, and reliability factors of the P_β average structure. Table 4 lists the interatomic distances and some selected bond angles.

Gamma Polymorph (P_γ). The X-ray diffraction pattern obtained for P_γ shows well-resolved splitting of the main Bragg reflections, demonstrating that the symmetry is still lower than

Table 1. Unit Cell, Positional, and Displacement Parameters for P_α in the Monoclinic *C*2/*c* Space Group, from Joint NPD and SXRPD Data at 295 K

unit cell parameters		reliability factors	NPD	SXRPD
a (Å)	10.15239(2)	R_p (%)	7.7	15.9
b (Å)	5.82242(1)	R_{wp} (%)	8.1	8.7
c (Å)	10.13798(1)	R_{exp} (%)	5.24	2.63
β (deg)	108.7285(1)	χ^2	2.41	10.9
vol (Å^3)	567.54(1)	R_{Bragg} (%)	3.06	5.8

atom	Wyckoff site	*x*/*a*	*y*/*b*	*z*/*c*	B_{eq} (Å^2)
Pb	8f	0.1307(1)	0.7804(2)	0.1269(2)	1.01(2)
Tm	4e	0	0.2535(3)	1/4	0.48(3)
Sb	4c	1/4	1/4	0	0.28(3)
O1	8f	0.1030(2)	0.2108(4)	0.0884(2)	0.94(2)
O2	8f	0.1458(2)	0.0344(4)	0.8524(2)	1.20(3)
O3	8f	0.3461(2)	0.0123(5)	0.6159(2)	1.23(3)

	anisotropic thermal factors ($\times 10^4$)					
atom	β_{11}	β_{22}	β_{33}	β_{12}	β_{13}	β_{23}
Pb	28.1(1)	65.2(3)	28.4(1)	−2.6(1)	6.9(1)	1.4(2)
Tm	7.9(2)	57.0(8)	7.0(3)	0	−2.4(2)	0
Sb	14.4(3)	5.5(9)	10.7(3)	−2.9(3)	9.9(2)	0.3(3)
O1	27.2(2)	79.6(5)	28.3(2)	5.8(3)	20.8(1)	−3.9(3)
O2	47.4(3)	75.0(7)	21.7(2)	−25.0(3)	9.3(2)	−14.5(2)
O3	19.9(2)	93.6(6)	41.0(3)	−19.0(3.2)	3.6(2)	−32.4(3)

Table 2. Main Interatomic Distances (Å) and Angles (deg) for P_α in the Monoclinic *C*2/*c* Space Group from Joint NPD/SXRPD Data at 295 K

	P_α
PbO_{12} Polyhedra	
Pb−O_1	3.341(3)[a]
Pb−O_1	2.538(3)
Pb−O_1	2.660(2)
Pb−O_1	3.285(2)[a]
Pb−O_2	3.198(3)[a]
Pb−O_2	3.077(3)
Pb−O_2	2.487(3)
Pb−O_2	2.871(3)
Pb−O_3	2.531(3)
Pb−O_3	2.988(3)
Pb−O_3	3.060(3)
Pb−O_3	3.326(3)[a]
⟨Pb−O⟩	2.95
$\langle Pb-O\rangle_{short}$	2.78
TmO_6 Octahedra	
Tm−O_1 (×2)	2.222(2)
Tm−O_2 (×2)	2.257(2)
Tm−O_3 (×2)	2.187(2)
⟨Tm−O⟩	2.22
O1−Tm−O1	167.1(2)
O2−Tm−O2	84.1(1)
O3−Tm−O3	102.9(1)
O1−Tm−O2	88.4(1)
O1−Tm−O2	82.1(1)
O1−Tm−O3	96.7(1)
O1−Tm−O3	91.3(1)
SbO_6 Octahedra	
Sb−O_1 (×2)	1.986(2)
Sb−O_2 (×2)	1.979(2)
Sb−O_3 (×2)	1.982(6)
⟨Sb−O⟩	1.98
O1−Sb−O1	180.0(2)
O2−Sb−O2	180.0(2)
O3−Sb−O3	180.0(2)
O1−Sb−O2	88.4(1)
O1−Sb−O2	91.6(1)
O1−Sb−O3	86.7(2)
O1−Sb−O3	93.3(2)
Angles around O	
Tm−O_1−Sb	156.9(1)
Tm−O_2−Sb	158.6(1)
Tm−O_3−Sb	165.1(1)
θ_A	−11.1
θ_B	−9.5
θ_C	−9.1

[a] Distance disregarded.

cubic (see Figure S.4). Some additional lines are indicative of the Tm/Sb long-range ordering, which is preserved at this temperature. These superlattice diffraction lines are of low intensity due to the small difference in the X-ray scattering power between Tm and Sb atoms. Some trial XRPD refinements have been carried out to determine the correct space group of P_γ. The possible space groups obtained from the SPUDS program[30] were the *I*4/*m* ($a^0a^0c^-$), the monoclinic *I*2/*m* ($a^0b^-b^-$), and the rhombohedral $R\bar{3}$ ($a^-a^-a^-$). A close inspection of the main peak splitting has ruled out both *I*4/*m* and *I*2/*m* as possible space groups (see inset of Figure S.4). First, the basic (400) would be split in both *I*4/*m* and *I*2/*m*, but it clearly remains as one single peak; only the splitting due to $K_{\alpha1}$ and $K_{\alpha2}$ radiations is resolved. In addition, trial Rietveld refinements in the *I*4/*m* and *I*2/*m* space groups were unsuccessful because no convergence was reached. The space group $R\bar{3}$ satisfactorily indexed all the peaks. The basic (222) diffraction line splits into two

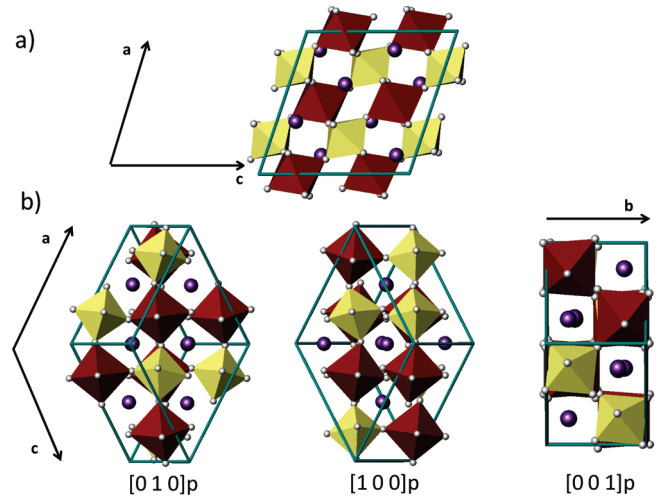

Figure 6. A projected view of the *C*2/*c* unit cell along the (a) [010] monoclinic direction and (b) the three pseudocubic axes [100], [010], and [001].

Table 3. Unit Cell, Positional, and Thermal Parameters for P_β, P_γ, and P_δ in the Monoclinic $P2_1/n$, Rhombohedral $R\bar{3}$, and Cubic $Fm\bar{3}m$ Space Groups, from NPD Data at 400, 438, and 463 K, Respectively

	P_β	P_γ	P_δ
a (Å)	8.2679(1)	5.8679(2)	8.3114 (1)
b (Å)	5.8444(1)	=*a*	=*a*
c (Å)	5.9007(1)	=*a*	=*a*
β (deg)	90.172(1)	60.081(2)	90.0000
V (Å^3)	285.13(1)	429.76(2)	574.15(2)
Pb	4e (*xyz*)	2c (*xxx*)	32f (*xxx*)
x	0.252(1)	0.249(2)	0.2470(1)
y	0.503(2)	0.249(2)	0.2470(1)
z	−0.002(1)	0.249(2)	0.2470(1)
B/Å^2	4.2(1)	3.5(4)	3.6(1)
Tm	2d (000)	1a (000)	4a (000)
B/Å^2	2.0(1)	2.2(1)	2.3(1)
Occ	1.00	1.00	1.00
Sb	2c ($^1/_2$00)	1b ($^1/_2{}^1/_2{}^1/_2$)	4b ($^1/_2$00)
B/Å^2	1.2(1)	1.5(1)	1.4(1)
Occ	1.00	1.00	1.00
O1	4e (*xyz*)	6f (*xyz*)	24e (*x*00)
x	0.765(1)	−0.239(3)	0.2648(2)
y	0.491(2)	0.263(3)	
z	0.550(1)	−0.287(2)	
B/Å^2	3.0(2)	3.9(3)	4.2(3)
O2	4e (*xyz*)		
x	0.029(1)		
y	0.261(1)		
z	0.736(2)		
B/Å^2	3.8(3)		
O3	4e (*xyz*)		
x	0.024(2)		
y	0.738(2)		
z	0.729(2)		
B/Å^2	3.7(3)		
reliability factors			
R_p (%)	17.2	22.3	24.6
R_{wp} (%)	12.3	17.3	16.8
R_{exp} (%)	5.61	13.3	12.6
χ^2	4.82	1.70	1.79
R_B (%)	5.92	5.06	5.23

peaks, indexed as (400) and (444) in $R\bar{3}$. From this evidence, the rhombohedral $R\bar{3}$ space group was selected to describe the P_γ structure.

The final structural refinement of the P_γ polymorph was carried out from NPD data at 438 K, corresponding to the

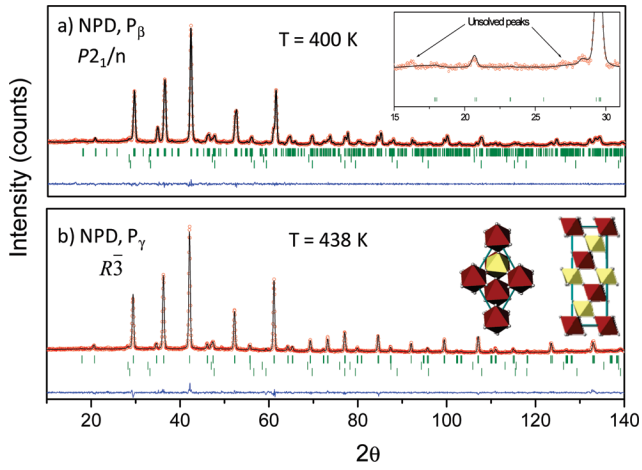

Figure 7. Observed (red ●), calculated (solid line), and difference (bottom) profiles after a Rietveld refinement of the NPD data for: (a) P_β polymorph measured at 400 K. The inset shows the unsolved incommensurate peaks. (b) P_γ polymorph measured at 438 K. The inset shows the schematic view of the rhombohedral $R\bar{3}$ crystal structure.

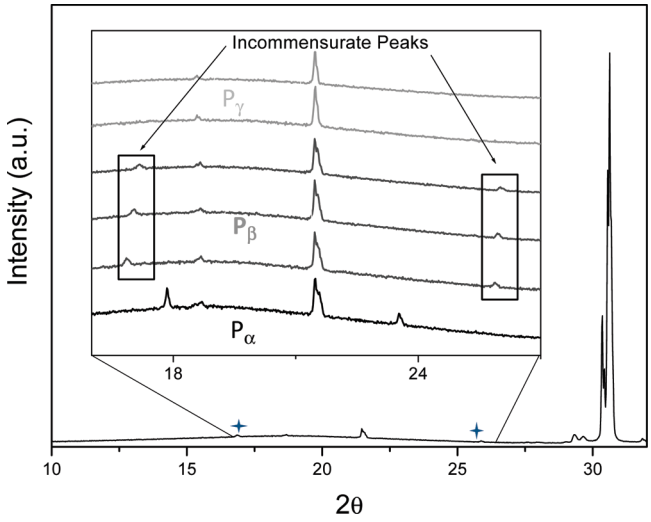

Figure 8. XRPD pattern of P_β. Inset: Thermal evolution of the incommensurate peaks between $T1$ and $T2$.

temperature region at the plateau between $T2$ and $T3$ observed at the DSC curve (Figure 2). Because of the narrowness of this zone, a study of the thermal evolution of the unit-cell parameters of this polymorph has not been carried out. Figure 7b shows the Rietveld plot of P_γ, where an excellent fit between observed and calculated patterns is shown. The unit-cell parameters obtained from the refinement, $a = b = c = 5.8679(1)$ Å and $\alpha = \beta = \gamma = 60.081(2)$, correspond to a slight rhombohedral distortion of the double perovskite; these parameters are related to the a_0 aristotype as $a = b = c \approx \sqrt{2}a_0$. In the structural model, Pb atoms occupy the general positions 2c (xxx), while the Tm and Sb atoms occupy the 1a (000) and 1b ($^1/_2{}^1/_2{}^1/_2$) Wyckoff sites, respectively. Finally, only one oxygen atom at the 6f (xyz) position is required to complete the octahedral sublattice. The crystal structure of P_γ is easily derived from the simple-cubic aristotype by combining the 1:1 long-range arrangement of the TmO_6 and SbO_6 units with an octahedral tilting around the 3-fold $[111]_p$-axis, resulting in the rhombohedral symmetry $a^-a^-a^-$. The inset of Figure 7b shows a schematic view of this rhombohedral polymorph. Table 3 contains the unit-cell parameters, atomic positions, isotropic thermal factors, occupancy, and reliability factors. Table 4 includes the interatomic distances and some selected bond angles.

Table 4. Main Interatomic Distances (Å) and Angles (deg) for P_β, P_γ, and P_δ from NPD Data at 400, 438, and 463 K, Respectively

	P_β	P_γ	P_δ
PbO_{12} Polyhedra			
Pb−O_1	3.24(1)[a]	(×3) 2.94(3)	(×6) 2.941(5)
Pb−O_1	2.67(1)	(×3) 2.80(1)	(×3) 2.902(5)
Pb−O_1	2.90(2)	(×3) 2.95(3)	(×3) 2.983(5)
Pb−O_1	2.97(2)	(×3) 3.08(1)	
Pb−O_2	2.79(1)		
Pb−O_2	2.73(1)		
Pb−O_2	3.13(1)[a]		
Pb−O_2	3.09(1)		
Pb−O_3	2.82(1)		
Pb−O_3	2.76(1)		
Pb−O_3	3.13(2)[a]		
Pb−O_3	3.03(2)		
⟨Pb−O⟩	2.94	2.94	2.95
$\langle Pb-O\rangle_{short}$	2.86		
TmO_6 Octahedra			
Tm−O_1 (×2)	2.21(1)	(×6) 2.19(1)	(×6) 2.202(2)
Tm−O_2 (×2)	2.20(1)		
Tm−O_3 (×2)	2.22(1)		
⟨Tm−O⟩	2.21	2.19	2.202
Angles around Tm			
O1−Tm−O1	180.0(5)	180.0(1)	180.0(1)
O1−Tm−O2	91.9(5)	90.2(8)	
O1−Tm−O2	88.1(5)		
O1−Tm−O3	88.7(6)		
O1−Tm−O3	91.3(6)		
SbO_6 Octahedra			
Sb−O_1 (×2)	1.97(1)	(×6) 1.97(1)	(×6) 1.954(2)
Sb−O_2 (×2)	1.98(1)		
Sb−O_3 (×2)	1.95(1)		
⟨Sb−O⟩	1.97	1.97	1.954
Angles around Sb			
O1−Sb−O1	180.0(5)	180.0(1)	180.0(1)
O1−Sb−O2	90.3(6)	90.2(6)	
O1−Sb−O2	89.7(6)		
O1−Sb−O3	89.2(6)		
O1−Sb−O3	90.8(7)		
Angles around O			
Tm−O_1−Sb	163.4(2)	(×3) 172.2(1)	180.0(1)
Tm−O_2−Sb	166.6(3)		180.0(1)
Tm−O_3−Sb	168.7(4)		
θ_A	−7.5	−3.9	0
θ_B	−7	−3.9	0
θ_C	6	−3.9	0

[a] Distance disregarded.

Delta Polymorph (P_δ). The last polymorph found in the high-temperature sequence of Pb_2TmSbO_6 is the expected cubic double perovskite; it constitutes one more example of the many double perovskites finishing their thermal evolution in the well-known $Fm\bar{3}m$ space group. The structural refinement from the high-resolution NPD data for P_δ was performed in the $Fm\bar{3}m$ space group (No. 225). In this model, Tm and Sb atoms were located at the 4a (000) and 4b ($^1/_2$00) Wyckoff sites, respectively. O atoms are placed at the 24e sites (x00), and Pb atoms occupy the 32f (xxx) positions, presenting a subtle off-center displacement along the [111] direction, similar to that reported for Pb_2ScSbO_6.[31] This structure is commonly adopted by 1:1 long-range ordered double perovskites[32−35] that contain untilted BO_6 octahedra, corresponding to the $a^0a^0a^0$ Glazer notation. The Rietveld plot after the NPD refinement is displayed in Figure

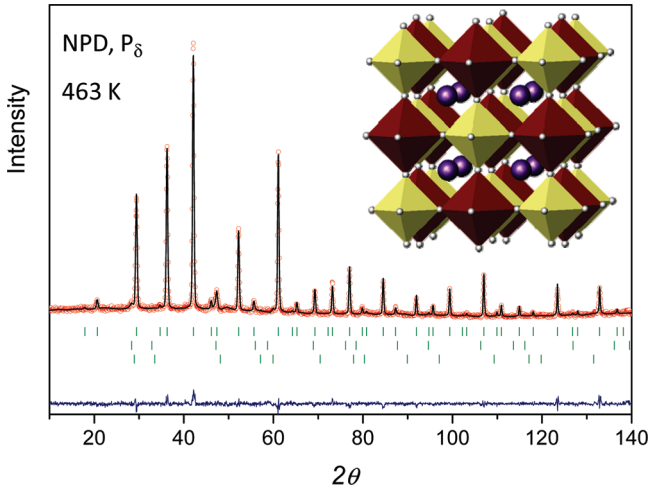

Figure 9. Observed (red ●), calculated (solid line), and difference (bottom) profiles after a Rietveld refinement of the NPD data for P_δ polymorph measured at 463 K. The inset shows the schematic view of the cubic $Fm\bar{3}m$ crystal structure.

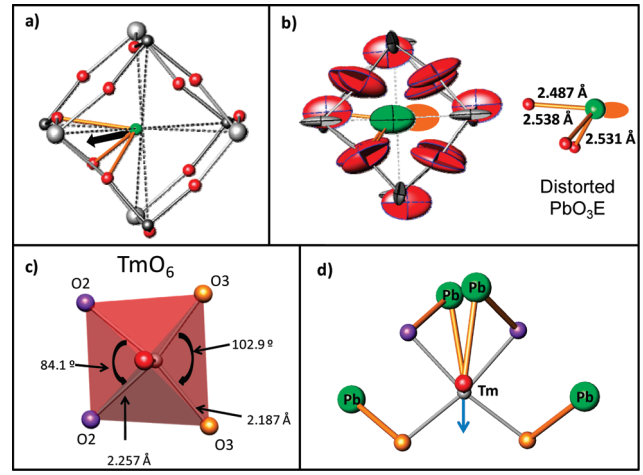

Figure 10. (a) Schematic view highlighting the displacement of a lead atom in the void between eight octahedra for the alpha polymorph, with atomic isotropic thermal factors. (b) PbO_{12} void represented with anisotropic thermal factors and the simplified PbO_3E environment for the lead atoms. The possible orientation of the $6s^2$ lone pair is indicated. (c) Representation of the angles and distances of TmO_6 octahedra in P_α. (d) Tm polyhedron and the interactions with the nearest lead atoms via common oxygens.

9; Table 3 shows the determined unit-cell parameters, atomic positions, isotropic thermal factors, occupancy, and reliability factors. Table 4 contains the main bond lengths and some selected bond angles.

It is worth mentioning that during the structural refinements of all the polymorphs the possibility of antisite disorder of the two B-type cations was investigated. Without exception, the refinements indicated a complete ordering of Tm and Sb cations over the two B sites. This is expected from the large size difference between Tm^{3+} and Sb^{5+} cations. On the other hand, the refinement of the oxygen site fractional occupancies gave a value of unity (within the standard deviations) for all the cases; hence, the occupancies were subsequently fixed to this value. The temperature-dependent NPD Rietveld plots are included in the Supporting Information as Figure S.6 for P_α and Figure S.7 for P_β, because only one pattern has been refined for the gamma and delta polymorphs.

4. Discussion

The room-temperature P_α polymorph is the first case of a double perovskite (with two different cations at the B-sublattice) defined in the *C*2/*c* space group. Only a few examples of highly distorted *C*2/*c* perovskites have been reported until now, that is, $BiMnO_3$ and $BiScO_3$,[36,37] both synthesized under high-pressure conditions. The crystal structure determined for P_α belongs to the $a^-b^-b^-$ tilt system. The characteristic tilting angles can be estimated as: $\theta_C = (180 - \phi_c)/2$ (where ϕ_c is the average Sb−O−Tm angle defined by O2 and O3), $\theta_B = (180 - \phi_b)/2$ (where ϕ_b is the average Sb−O−Tm angle for O1 and O3), and $\theta_A = (180 - \phi_a)/2$ (where ϕ_a is the average Sb−O−Tm angle for O1 and O2), where the subindices A, B, and C represent the pseudo cubic axis along which the tilt occurs. The obtained tilting angles where $\theta_A = -11.1$, $\theta_B = -9.5$, and $\theta_C = -9.1$.

In the distorted PbO_{12} polyhedron, the effective coordination of Pb ions can be considered as 8-fold (disregarding distances longer than 3.1 Å) with average distances $\langle Pb{-}O\rangle_{short}$ of 2.78 Å. These values are in reasonable agreement with those expected from the ionic radii sums[26] of 2.69 Å for $^{VIII}Pb^{2+}$ (i.r.: 1.29 Å) and $^{VI}O^{2-}$ (i.r.: 1.40 Å). Several lead-containing double perovskites present an off-center lead displacement, due to the asymmetry introduced by the polarization of the lone pair $6s^2$; this case is not the exception. From the distances presented in Table 2, a group of four shorter Pb−O distances reveals the direction of the displacement, which occurs toward four oxygen atoms of the aristotype following the direction established by the vector $[1^3/_5{}^2/_5]$ from the geometrical center of the void.

Figure 10a shows the environment of lead atoms with the displacement direction marked with an arrow. In addition, Figure 10b shows the environment represented by the anisotropic thermal factors of the atoms; an empty region is observed, and probably the 6s lone pair of lead atoms may occupy this unfilled void. In the group of the four shortest Pb−O bond lengths, three of them take values considerably lower than the fourth distance (2.5 vs 2.66 Å), in such a way that the displacement pattern generates a PbO_3E environment, where E represents the lone

(25) Chandra, A.; Ranjan, R.; Singh, D. P.; Khare, N. D.; Pandey, L. *J. Phys.: Condens. Matter* **2006**, *18*, 2977.
(26) Shannon, R. D. *Acta Crystallogr., Sect. A* **1976**, *32*, 751.
(27) Topas Academic. *General Profile and Structure Analysis Software for Powder Diffraction Data*; Bruker AXS: Karlsruhe, Germany, 2004.
(28) Hahn, T., Ed. *International Tables for Crystallography, Vol. A, "Space-group Symmetry"*; Published for International Union of Crystallography (IUCr) by D. Reidel Publishing Co.: Dordrecht, Holland, Boston, 1983; p 177.
(29) Favre-Nicolin, V.; Černý, R. *J. Appl. Crystallogr.* **2002**, *35*, 734.
(30) Lufaso, M. W.; Woodward, P. M. *Acta Crystallogr., Sect. B* **2001**, *57*, 725.
(31) Larrégola, S. A.; Alonso, J. A.; Pedregosa, J. C.; Martínez-Lope, M. J.; Algueró, M.; De La Peña-O'Shea, V.; Porcher, F.; Illas, F. *Dalton Trans.* **2009**, *28*, 5453.
(32) Kennedy, B. J.; Saines, P. J.; Kubota, Y.; Minakata, C.; Hano, H.; Kato, K.; Takata, M. *Mater. Res. Bull.* **2007**, *42*, 1875.
(33) Patwe, S. J.; Achary, S. N.; Mathews, M. D.; Tyagi, A. K. *J. Alloys Compd.* **2005**, *390*, 100.
(34) Martínez-Lope, M. J.; Alonso, J. A.; Casais, M. T. *Z. Naturforsch., B* **2003**, *58*, 571.
(35) Martínez-Lope, M. J.; Alonso, J. A.; Casais, M. T.; Fernández-Díaz, M. T. *Eur. J. Inorg. Chem.* **2002**, 2463.
(36) Yang, H.; Chi, Z. H.; Jiang, J. L.; Feng, W. J.; Cao, Z. E.; Xian, T.; Jin, C. Q.; Yu, R. C. *J. Alloys Compd.* **2008**, *461*, 1.
(37) Belik, A. A.; Iikubo, S.; Kodama, K.; Igawa, N.; Shamoto, S.; Maie, M.; Nagai, T.; Matsui, Y.; Yu, S.; Stefanovich; Lazoryak, B. I.; Takayama-Muromachi, E. *J. Am. Chem. Soc.* **2006**, *128*, 706.

pair (see Figure 10b). These unexpectedly short Pb−O bond lengths are consistent with the reported values for highly hybridized systems as PbO[38] and simple perovskites, which present a strong hybridization between Pb 6s-states and anion p-states, as $PbRuO_3$.[39,40] Theoretical calculations performed in PbO have demonstrated that the highly stereochemically active character of the $6s^2$ lone pair is a result of the interaction of the antibonding combination of Pb 6s and anion p states with unfilled Pb 6p orbitals. In the case of litharge PbO, this causes a shift of the states at the Fermi level to lower energy and the appearance of unoccupied Pb 6s states in the conduction band. It has been concluded that the highly hybridized Pb−O bonds are responsible for the extremely different experimental Pb−O bond lengths, and in the second term of the $6s^2$ electron pair behavior. The magnitude of the displacement calculated from the structural data was ${}^{\alpha}d_{Pb} = 0.506$ Å. Consequently, it can be concluded that the lone electron pair of Pb^{2+} cations is highly active in Pb_2TmSbO_6, resulting in the antiparallel displacement of Pb^{2+} ions from the centroids of their O coordination environments as it occurs in the isostructural compounds $BiScO_3$ and $BiMnO_3$.[36,37]

In addition, the refinement reveals the presence of a markedly irregular character of the octahedra, which present different sizes (see Table 2). The TmO_6 octahedron presents a Tm displacement from the center of the polyhedra (~0.156 Å) to an octahedron edge formed by O3 atoms, as deduced from the Tm−O distances and angles displayed at Table 2. In Figure 10c the asymmetry of the TmO_6 octahedron is clearly observed. The average ⟨Tm−O⟩ bond length obtained from the data of Table 2 was 2.22 Å, close to that calculated from the ionic radii sums (2.28 Å). On the other hand, the SbO_6 octahedron is more regular than TmO_6, without B-cation displacement, which is reflected in the similitude of the three Sb−O distances showed in Table 2. The average observed ⟨Sb−O⟩ distance is 1.98 Å, in agreement with that calculated of 2.00 Å. Both octahedral sites are different in symmetry. The Sb atom is located at a center of symmetry. Therefore, the O−Sb−O bond angles with the opposite oxygen atoms are constrained to be 180 by the space group symmetry, while the Tm site has only a 2-fold rotational symmetry.

To evaluate the octahedron distortion, the Δd parameter has been calculated, as defined by Halasyamani:[41]

$$\Delta d = \frac{||(M-O1) - (M-O2)||}{||\cos\langle O1-M-O2\rangle||} + \frac{||(M-O3) - (M-O4)||}{||\cos\langle O3-M-O4\rangle||} + \frac{||(M-O5) - (M-O6)||}{||\cos\langle O5-M-O6\rangle||}$$

where the pairs (O1,O2), (O3,O4), and (O5,O6) are the oxygen atoms that constitute the octahedron and are located in opposite positions from each other. The obtained value for the TmO_6 octahedron is ${}^{Tm}\Delta d = 0.143$, while for SbO_6 the obtained value is zero, because the defined couples of oxygen atoms occupy exactly opposite positions in the octahedron. The value obtained for TmO_6 falls into the first category defined by Halasyamani,[41] with a magnitude located in the range of $0.05 < \Delta d < 0.4$; following the criteria proposed by the author, this figure corresponds to a weak magnitude of octahedral distortion. It is interesting to note that in several cases the shifting of metals in octahedral coordination seems to appear due to the interaction with a lone-pair element, or with the oxygen anions that are linked to the lone-pair element. Tm atoms shift away from the oxide anions that present the two shorter Pb−O bond lengths (and are bridged by the same lead atom; see Figure 10d).

Several examples of distorted octahedra have been reported in the literature, and the causes of such distortion are different in nature. The most common cause is the existence of an electronic instability associated with the presence of a d^0 cation. In these cases, the distortion can be attributed to second-order Jahn−Teller (SOJT) effects. These effects occur when the empty d-orbitals of the metal mix with the filled p-orbitals of the oxide ligands. In extended structures, this mixing results from a spontaneous distortion of the metal cation that removes the near degeneracy of these two orbital sets, as it occurs in $PbTiO_3$.[42] A different cause of the octahedral distortion is that observed in $PbVO_3$,[43] which presents a highly distorted tetragonal perovskite structure ($c/a = 1.229$). In this case, the observation of such a distortion is driven by the tendency of V^{4+} cations to form a strongly distorted octahedral coordination with one short vanadyl V−O distance, which results in a 5-fold coordination of the V atoms, stabilizing a square pyramid VO_5 instead of the expected tridimensional framework of corner-shared octahedra. The magnitude of the B-cations displacement in both examples is near 0.5 Å, which is considerably larger than that presented by Tm atoms in the present case (0.15 Å). This fact plus the non-d^0 nature of Tm atoms reflects that in the Pb_2TmSbO_6 the TmO_6 octahedral distortion is produced by the interaction with the highly stereoactive lead atoms.

It must be pointed out that the results of theoretical calculations reported for $BiMnO_3$ by Seshadri et al.[44] show that the highly distorted $C2/c$ structure is associated with the stereoactivity of the highly polarized bismuth $6s^2$ lone pair, this being responsible for such seldom crystal structure. It can be assumed that Pb^{2+} ions in the P_α perovskite induce a behavior similar to that promoted by Bi^{3+} in the mentioned perovskite. On the other hand, it can be thought that the lone-pair activity is the consequence instead of the cause of the highly distorted crystal structure. In fact, as it has been pointed out in the former paragraph, in PbO the remarkable stereoactivity of the $6s^2$ lone pair is due to the presence of highly covalent bonding with oxygen atoms, which favors the $6s^2$ polarization.[38] Therefore, the distorted character of the crystal structure of P_α must be related to the highly covalent character of the shortest Pb−O bonds.

After T1, the P_β polymorph is stabilized; its crystal structure has been refined in the $P2_1/n$ space group (disregarding for the time being some very weak peaks incommensurate with the $P2_1/n$ cell). This average structure is a good approach that is worth describing, because it encloses the main features of the perovskite structure (octahedral tilting, B−O distances, and B−O−B angles). Its contains alternating TmO_6 and SbO_6 octahedra, displaying an in-phase octahedral tilting along the [001] direction of the pseudocubic cell, and an antiphase tilting

(38) Walsh, A.; Watson, G. W. *J. Solid State Chem.* **2005**, *178*, 1422.
(39) Cheng, J.-G.; Zhou, J.-S.; Goodenough, J. B. *Phys. Rev. B* **2009**, *80*, 174426.
(40) Kimber, S. A. J.; Rodgers, J. A.; Wu, H.; Murray, C. A.; Argyriou, D. N.; Fitch, A. N.; Khomskii, D. I.; Attfield, J. P. *Phys. Rev. Lett.* **2009**, *102*, 046409.
(41) Shiv Halasyamani, P. *Chem. Mater.* **2004**, *16*, 3586.
(42) Bergman, J. G.; Crane, G. R.; Turner, E. H. *J. Solid State Chem.* **1977**, *21*, 127.
(43) Shpanchenko, R. V.; Chernaya, V. V.; Tsirlin, A. A.; Chizhov, P. S.; Sklovsky, D. E.; Antipov, E. V.; Khlybov, E. P.; Pomjakushin, V.; Balagurov, A. M.; Medvedeva, J. E.; Kaul, E. E.; Geibel, C. *Chem. Mater.* **2004**, *16*, 3267.
(44) Seshadri, R.; Hill, N. A. *Chem. Mater.* **2001**, *13*, 2892.

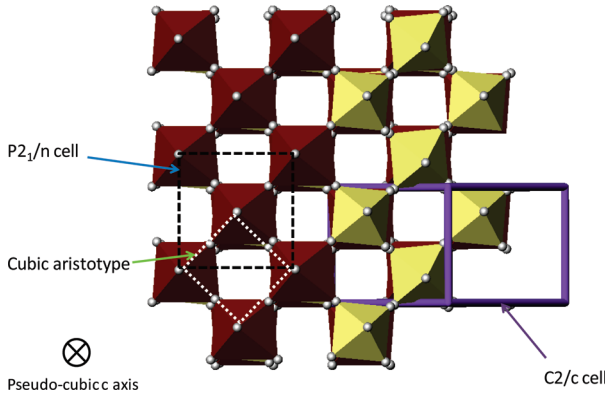

Figure 11. View of the *C*2/*c* structure along the *c* pseudocubic axis corresponding to the [−101] monoclinic direction. The *C*2/*c* unit cell is marked with a solid line; the [001] view of the monoclinic P2$_1$/n unit cell is displayed with a dark dashed line; and the cubic aristotype is indicated with a white dotted line.

along the [100] and [010] directions, corresponding to the $a^-a^-b^+$ Glazer notation as derived by Woodward[2] for 1:1 ordering in double perovskites. The tilting angles were calculated with the same criteria described for P_α, and the values obtained were $\theta_A = -7.5$, $\theta_B = -7$, and $\theta_C = 6$. From the data presented in Table 4, an increment in the symmetry of the octahedral and cuboctahedral sites is observed, in agreement with the global decrease of the tilting angles. For the lead polyhedron, this symmetry increase is indicated by the Pb−O bond lengths (Table 3). Disregarding bond lengths longer than 3.1 Å, the lead atoms coordination can be considered as 9-fold with an average Pb−O distance of 2.86 Å.

The calculated off-center lead displacement was about 0.02 Å in the P_β polymorph, derived from the small difference existing between the Pb−O bond lengths. This tiny displacement could correspond to an average position of Pb over the modulated crystal structure. This modulation could be, in fact, associated with the lead atoms positions due to the stereoactivity of these cations. In addition, the BO_6 octahedra become more regular in the P_β polymorph, as determined from the O−B−O angles (Table 3), which are really close to the expected ones for regular octahedra.

The first phase transition involves the transformation between P_α and P_β, which are related through the *c* pseudocubic axis, taking into account the tilt system adopted for both polymorphic phases (P_α $a^-b^-b^-$ and P_β $a^-a^-b^+$). The DSC peak observed at *T*1 can be assigned to the change of the sign of θ_C, going from an antiphase to an in-phase arrangement. Figure 11 shows the relationship between the pseudocubic *c*-axis of the unit cells adopted by P_α and P_β, around which the transition occurs. As it was previously mentioned, θ_C is determined by O2 and O3 positions. In Figure S.8, the thermal evolution of the average distances $\langle Tm-O_{2,3}\rangle$ and $\langle Sb-O_{2,3}\rangle$ and the angle $\langle Sb-O_{2,3}-Tm\rangle$ for P_α polymorph are shown. This figure shows the followed sequence previous to *T*1, and it can be seen that the tilt angle (or the Sb−O−Tm angle) decreases (increase) upon rising temperature. This expected fact is accompanied by an increment of the Tm−O bond length and the decrease of the Sb−O distances (see Figure S.8a).

The second phase transition is related to the unification of the three tilt angles from the former $P2_1/n$ ($a^-a^-b^+$) arrangement to the rhombohedral $R\bar{3}$ ($a^-a^-a^-$) system. The tilting angles calculated were $\theta_A = \theta_B = \theta_C = -4$. This merge of the tilting along the [111] pseudocubic direction induces the convergence of the previously defined O1, O2, and O3 monoclinic oxygen atoms to one oxygen atom in P_γ. This polymorph presents regular octahedra, with B−O bond lengths of 2.19 and 1.97 Å for TmO_6 and SbO_6, respectively. On the other hand, the PbO_{12} polyhedron presents four groups of three equivalent distances. Woodward[45] derived that in rhombohedral perovskites belonging to the $a^-a^-a^-$ tilt system the A cation must present a 9-fold coordination, where the three closest oxygen anions must form a perfect trigonal planar coordination in a plane perpendicular to the 3-fold axis, while the other six anions are arranged in a twisted trigonal prism about the A cation. In the case of P_γ, the rhombohedral distortion is very subtle ($a = 60.08$), so this pattern pointed out by Woodward tends to a cuboctahedral environment for the lead atoms. Consequently, the small differences that exist between the four groups of different bond lengths are a consequence of the subtle distortion. All the Pb−O bond lengths are shorter than 3.1 Å; thus 12 oxygen atoms are present in the first coordination sphere of lead atoms taking the average value of 2.94 Å. A minor lead displacement can be derived from the analysis of the Pb−O bond lengths: First, it must be pointed out that the greater and smaller Pb−O distances are not related to the displacement because they cancel to each other, so the displacement occurs toward a TmO_6 face of three oxygen atoms, and the calculated shift is 0.02 Å.

The second phase transition from P_β to P_γ is characterized by the transition from the $a^-a^-b^+$ tilt system to the $a^-a^-a^-$ arrangement. In agreement with the magnitude of the DSC peaks, this fact involves a large energy transfer because all the tilting angles are concerned. θ_A and θ_B present a slight decrease from −7 to −4 , while θ_C presents the most abrupt modification, because it changes from in-phase to antiphase.

Finally, the last polymorph (P_δ) adopts a characteristic cubic double perovskite structure, which can be viewed as an ordered stacking of TmO_6 and SbO_6 octahedra sharing corners without any tilting. Moreover, the space group symmetry ($Fm\bar{3}m$) imposes a total regularity of the octahedral sites (see Table 4). The refined Tm−O and Sb−O bond lengths are 2.202(2) and 1.954(2) Å, respectively. On the other hand, the lead atoms occupy the voids between every 8 octahedra, exhibiting 12-fold oxygen coordination. The observed Pb−O distances listed in Table 4 can be separated into three groups: the first one consists of three similar bonds, which present the shortest Pb−O bond length of 2.902(5) Å; the second group presents the three longest bond lengths, of 2.983(5) Å; and finally we have a plane of six similar Pb−O bonds (equatorial plane) that compose the last group and adopt intermediate values of 2.941(5) Å. A lead displacement of 0.14 Å is observed along the [111] cubic direction, toward a TmO_6 face formed by three oxygen atoms. The average ⟨Pb−O⟩ value of 2.952 Å is slightly larger than that expected from the tabulated ionic radii (at RT), which must be a result of the thermal expansion of the cell.

Figure 12 shows the thermal evolution of the unit-cell parameters across the four polymorphs normalized to the cubic aristotype a_0 (Figure 12a) and the tilting angles (Figure 12b). The three DSC peaks are associated with important modifications of the unit-cell parameters. After the first structural transition, *a* and *c* diverge from each other, whereas *a* and *b* converge as temperature increases; this fact is accompanied by the change in the sense of the tilting angle θ_C, while both θ_A and θ_B approximate to each other. At *T*2 the merging of the unit-cell parameters and the tilting angles is observed, giving

(45) Woodward, P. M. *Acta Crystallogr., Sect. B* **1997**, *53*, 44.

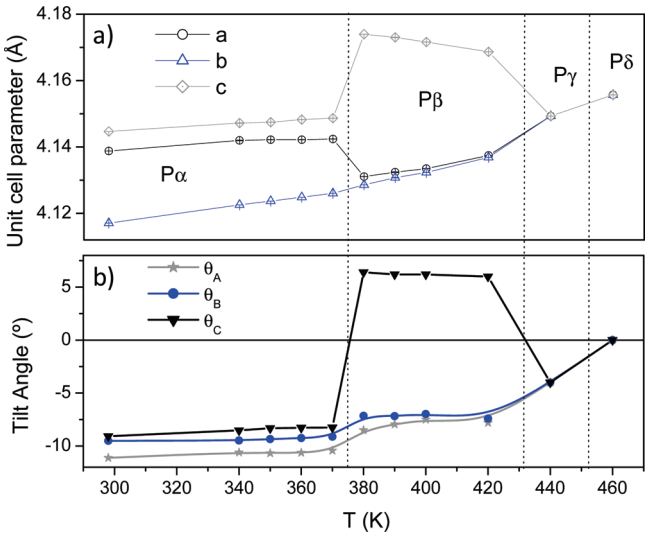

Figure 12. Thermal evolution for the whole investigated temperature range of (a) the unit-cell parameters taking into account the existent relationship with the aristotype and (b) the three tilting angles θ_A, θ_B, and θ_C through the [100], [010], and [001] pseudocubic directions, respectively. In both cases, the transition temperatures are indicated with dotted lines.

rise to a subtle rhombohedral distortion. This process involves another change of sense of θ_C, engaging the most energetic event revealed by the DSC experiment. Finally, the convergence between all the unit-cell parameters and the disappearance of the octahedral tilting is achieved when the cubic P_δ polymorph is formed.

Additionally, the enthalpies calculated from the DSC peaks ($\Delta_1H = 813$ J/mol, $\Delta_2H = 1425$ J/mol, and $\Delta_3H = 114.4$ J/mol) suggest that all the phase transitions just involve the overcoming of electrostatic potential barriers, due to the displacive nature of phase transitions in perovskites. The phase transition succession presented on increasing temperature follows the sequence $C2/c \rightarrow P2_1/n \rightarrow R\bar{3} \rightarrow Fm\bar{3}m$, which constitutes a novel sequence in the high-temperature evolution of perovskite oxides. From the intensity of the DSC peaks, it is evident that the first and the second phase transitions, which involve changes of sign of θ_C (from antiphase to in-phase configurations), engage higher energetic barriers, going through a completely eclipsed arrangement of adjacent octahedra along the $[001]_p$ direction of the structure. This generates a structural boundary that requires a relatively important energy contribution to be overcome.

5. Conclusions

Pb_2TmSbO_6 is the first example of a highly distorted $C2/c$ perovskite structure that has been obtained at ambient pressure. The room-temperature crystal structure of this novel double perovskite has been determined ab initio and refined from NPD and SXRPD data. This perovskite superstructure combines the long-range ordering of Tm and Sb cations over the B positions, and a tilting in antiphase of TmO_6 and SbO_6 octahedra along the three pseudocubic directions, with the scheme $a^-b^-b^-$. $BiScO_3$ and the multiferroic $BiMnO_3$ oxides are the only examples of this kind of perovskite superstructure; both must be stabilized under high-pressure conditions. Some particular structural features unveil the high stereochemical activity presented by the $6s^2$ lone pair of Pb^{2+}, first in the RT structure, which is polarized and induces a lead displacement from the center of the polyhedron of about 0.506 Å. Also, Tm atoms show a shifting from the center of the TmO_6 octahedra in 0.15 Å toward an edge probably due to the asymmetric interaction between the three different oxygen and lead atoms. The thermal evolution study of the crystal structure, investigated from NPD data, shows the existence of four polymorphic phases of Pb_2TmSbO_6 composition. The tilting progression observed on heating is $a^-b^-b^- \rightarrow a^-a^-b^+ \rightarrow a^-a^-a^- \rightarrow a^0a^0a^0$. The space group succession, $C2/c \rightarrow P2_1/n \rightarrow R\bar{3} \rightarrow Fm\bar{3}m$, constitutes a novel sequence in the high-temperature evolution of the crystal structures of the double perovskite oxides. The structural features are in agreement with the transition enthalpies determined from DSC measurements, because the most energetic phase transitions involve the change of sign of the θ_C tilting angle.

Acknowledgment. S.A.L. is thankful for a CONICET fellowship. J.C.P. thanks CONICET (Project PIP No 2008-01360), SECyT-UNSL (Project 7707), and ANPCYT (Project PICT 25459). J.C.P. is member of CONICET. J.A.A. acknowledges the financial support of the Spanish Ministry of Education to the project MAT2007-60536. We are grateful to PSI for making all facilities available.

Supporting Information Available: Figures S1−S8 and Table SI. This material is available free of charge via the Internet at http://pubs.acs.org.

JA104417F